Optimization of the Signal-to-Background Ratio in Prompt Gamma Imaging Using Energy and Shifting Time-of-Flight Discrimination: Experiments With a Scanning Parallel-Slit Collimator

Patricia Cambraia Lopes, Paulo Crespo, Jan Huizenga, and Dennis R. Schaart

***Abstract*—Much attention is currently being paid to imaging prompt gamma (PG) rays for *in vivo* proton range monitoring in proton therapy. PG imaging using a collimator is affected by neutron-related background. We study the effectiveness of background reduction experimentally, using a scanning parallel-slit PG collimator as a simplified model of a multislat PG camera. The analysis is focused on the falloff region of the PG intensity profile near the Bragg peak, which is the typical region of interest for proton range estimation. Background reduction was studied for different energy windows, with and without a shifting time-of-flight window that takes into account the proton velocity within the phantom. Practical methods are put forward that apply to cyclotron-based pencil beams. The parallel-slit collimator was placed in front of arrays of cerium-doped lutetium yttrium silicate-coupled digital silicon photomultipliers, used to measure energy and time spectra together with intensity profiles of prompt events emitted from a polymethylmethacrylate phantom irradiated with a 160-MeV proton pencil beam. The best signal-to-background ratio of ∼1.6 was similar to that obtained previously with a knife-edge-slit collimator. However, the slope-over-noise ratio in the PG-profile falloff region, was ∼1.2 higher for the present collimator, given its better resolution.**

***Index Terms*—Digital silicon photomultipliers, parallel-slit collimator, prompt gamma imaging, shifting time-of-flight discrimination.**

I. Introduction

IN VIVO monitoring of the proton range is currently a very active field of research in proton therapy, as most of the therapeutic effect of a proton beam is localized at its endpoint, where a maximum of energy (the Bragg peak) is imparted to the medium with nearly no dose deposited beyond that point. Much attention is currently being paid to the use of prompt gamma (PG) rays that are emitted along the beam path as a result of nuclear interactions between the protons and the irradiated medium. Due to the prompt nature of their emission, PGs can potentially provide valuable feedback on the treatment delivery in real-time and for individual pencil beams.

It is of importance to suppress the large amount of background counts present in PG images, resulting directly and/or indirectly from the simultaneously created neutrons. Testa *et al.* [17] were the first to apply a time-of-flight (TOF) technique to reduce neutron-related background in PG imaging with a collimated detector, upon irradiation with 73-MeV/u carbon ions. Such TOF discrimination is based on the principle that neutrons travel slower than (massless) gamma quanta. Using time-resolved Monte Carlo simulations, Biegun *et al.* [2] proposed a general method to improve the effectiveness of TOF discrimination in PG detection, based on a shifting TOF acceptance window. The optimum TOF shift depends on the beam energy and the proton penetration depth, as it includes the travel time of the proton beam through the patient up to the PG emission-point being imaged. Golnik *et al.* [8] have further extrapolated these principles and have proposed a so-called PG timing method for range assessment, based on observables taken from the time-spectrum of PGs emitted along the entire particle path obtained from a single uncollimated point measurement.

This paper focuses on PG imaging with (mechanical) collimation. PG images or intensity profiles can be obtained in a straightforward way by projection through a collimator,

Manuscript received January 22, 2018; revised April 2, 2018; accepted June 7, 2018. Date of publication June 14, 2018; date of current version August 31, 2018. This work was supported in part by the Foundation for Fundamental Research on Matter, The Netherlands, under Grant 09NIG18, and in part by the European Union Seventh Framework Program under Grant 241851 and Grant 264552. The work of P. Cambraia Lopes was supported by the Fundação para a Ciência e a Tecnologia, Lisbon, Portugal, through the European Social Fund and Programa Operacional Potencial Humano under Grant SFRH/BD/73705/2010. The work of P. Crespo was supported in part by the Fundação para a Ciência e a Tecnologia, Lisbon, Portugal, through the European Social Fund and Programa Operacional Potencial Humano under Grant SFRH/BPD/39223/2007, and in part by the QREN—FEDER through the Sistema de Incentivos à Investigação e Desenvolvimento Tecnológico under Grant CENTRO-07-ST24-FEDER-002007 (Project "Radiation for Life"). *(Corresponding author: Patricia Cambraia Lopes.)*

P. Cambraia Lopes is with the Department of Radiation Science and Technology, Delft University of Technology, 2629 JB Delft, The Netherlands, also with the Laboratório de Instrumentação e Física Experimental de Partículas, Universidade de Coimbra, 3004-516 Coimbra, Portugal, and also with the Heidelberg Ion-Beam Therapy Center, Heidelberg University Clinic, 69120 Heidelberg, Germany (e-mail: patitacambraia@gmail.com).

P. Crespo is with the Laboratório de Instrumentação e Física Experimental de Partículas, Universidade de Coimbra, 3004-516 Coimbra, Portugal, and also with the Department of Physics, Universidade de Coimbra, 3004-516 Coimbra, Portugal.

J. Huizenga is with the Department of Radiation Science and Technology, Delft University of Technology, 2629 JB Delft, The Netherlands.

D. R. Schaart is with the Department of Radiation Science and Technology, Delft University of Technology, 2629 JB Delft, The Netherlands, and also with Holland Proton Therapy Center, 2629 JH Delft, The Netherlands (e-mail: d.r.schaart@tudelft.nl).

Color versions of one or more of the figures in this paper are available online at http://ieeexplore.ieee.org.

Digital Object Identifier 10.1109/TRPMS.2018.2846612

which only accepts rays emitted at certain angles, thus providing spatial information. In the context of proton therapy, experimental studies with collimator-based PG imaging systems have shown that TOF discrimination improves the signal-to-background (S/B) ratio, even with a relatively broad time window (4-ns width [14]) or a relatively small (i.e., to what can be practically achieved) distance between the collimator and the beam [3]. The S/B improvement directly translates into a reduced uncertainty in the estimated falloff position of the PG longitudinal profile, which is correlated to the proton range. First TOF-based studies have imaged PGs with a point detector coupled to a single-parallel-slit collimator, placed at 20-cm distance (front-surface) [14] or 40-cm distance from the beam [13]. Lopes *et al.* [3] instead used a knife-edge slit collimator similar to [16], placed at only 13 cm from the beam, to image about 66 mm of the beam axis using a pixelated scintillation detector. In [3], TOF calibration was applied on a per-segment basis and a fine TOF window was used (viz., 1.5-ns width).

In all of the aforementioned experiments, the time stamps (TSs) could be retrieved relative to a given phase of the cyclotron radiofrequency (RF) signal, due to the fact that bunches of protons are delivered synchronously to the RF cycle. This is also the case in this paper. The time spread of protons within the RF cycle (bunch width $\gtrsim$ 1-ns full width at half maximum (FWHM)) imposes a lower limit on the width of the TOF window and, therefore, on the achievable background reduction [2]. The distance between the collimator and the beam also imposes a limit on the effectiveness of TOF background rejection, as it influences the degree of overlap between the arrival times of the PGs and the neutron-induced background.

In this paper, we quantify the degree of background reduction that can be achieved by applying energy discrimination and the shifting TOF window introduced by Biegun *et al.* [2] to PG profiles measured with a parallel-slit collimator scanned along the beam axis. We focus on the falloff region of the PG intensity profile near the Bragg peak, which is the typical region of interest for estimating the proton range *in vivo*. We describe a method to apply experimentally the shifting TOF technique for background rejection. The scanning parallel-slit collimator may be seen as a simple model of a multislat collimator (also named multislit [11]) in what concerns the timing information. Thus, the method presented may be applied in more complex systems as well. In addition, we perform a direct comparison of experimental PG profiles, using TOF rejection, between a knife-edge collimator and a parallel-slit collimator. In particular, we compare the slope-over-noise ratio in the falloff of the PG profiles from the two collimators. This may be a good indicator of range estimation performance of a collimator in a homogeneous phantom, as it puts both system resolution and statistical noise into equation. The methodology and analysis presented constitute valuable tools for the development of clinical PG imaging systems based on such collimators.

II. Experimental Setup

The experiment was conducted at the West German Proton Therapy Center Essen, using a similar experimental setup as described in [3], except that a parallel-slit collimator was used instead of a knife-edge slit collimator. A detector based on Philips digital photon counters (DPCs [4], [6], [7]) coupled to cerium-doped lutetium yttrium silicate [LYSO:Ce, $Lu_{1.8}Y_{0.2}SiO_5(Ce)$] crystals was used because of its good time resolution (time resolution $<$ 255-ps FWHM for $>$ 511-keV photons with present settings).

In brief, the detector module (DPC-MO-22-3200 [5], [9]) had a total surface area of 68 mm $\times$ 68 mm and contained 8 $\times$ 8 DPC pixels at a pitch of 4 mm, each pixel containing 3200 single-photon avalanche diodes or microcells. A total of 256 pixelated LYSO:Ce crystals, with dimensions of 3.8 mm $\times$ 3.8 mm $\times$ 22 mm, were optically coupled 1-to-1 to the pixels.

The basic DPC functional unit consists of an arrangement of 2 $\times$ 2 DPC-pixels, the so-called DPC-chip, which incorporates two interleaved time-to-digital converters (TDCs) for TS generation, and readout electronics [6]. Upon readout of a valid event, the DPC-chip outputs the (digital) number of fired cells on each of its four pixels, as well as a a TS.

The detector acquisition electronics were synchronized with the cyclotron operating RF, i.e., instead of the internal 200-MHz clock an external reference clock was used, derived from the 106-MHz RF wave. In this way, the registration time of each event relative to the phase of the RF cycle could be obtained directly from the TDCs on the DPC-chip and TOF discrimination could be applied offline. For the detailed DPC-acquisition settings and conditions of operation used in this paper, the interested reader is referred to [3].

A polymethylmethacrylate (PMMA, $(C_5O_2H_8)_n$) phantom with dimensions of $\varnothing$15 cm $\times$ 20 cm was irradiated using a proton pencil beam with 160-MeV energy, a beam current of $\sim$10 pA, and $\sim 6.5\times10^9$ protons per measurement ($\sim$100 s long) at the exit of the beam nozzle. This corresponded to an administered dose of about 10 Gy at the Bragg peak. An additional two measurements of longer duration and equal beam current were performed in order to visualize the energy spectra and the per-pixel intensity maps with five times higher statistics. As in [3], a low beam current was used, due to the fact that the DPC data acquisition electronics used was part of a technology demonstrator kit that is not designed for high count rates. In particular, it makes use of a USB 2.0 connection to the readout computer, which forms a bandwidth bottleneck. It is noted that the use of a low beam current does not affect the conclusions of this paper.

Fig. 1 presents the geometrical arrangement (left) and a photograph (right) of the experimental setup. We performed nine point measurements with the collimated camera accepting events emitted at right angles from various proton penetration depths spanning between 12.2 and 17.2 cm (the proton range R of 160-MeV protons in PMMA equals 15.2 cm, defined as the distal position at which the depth-dose profile has reduced to 80% of the maximum height). In order to measure at different depths, the phantom was translated longitudinally along the beam axis. The corresponding changes in proton travel time through air between measurements were corrected for, so that the experiment was equivalent to moving the detector + slit.

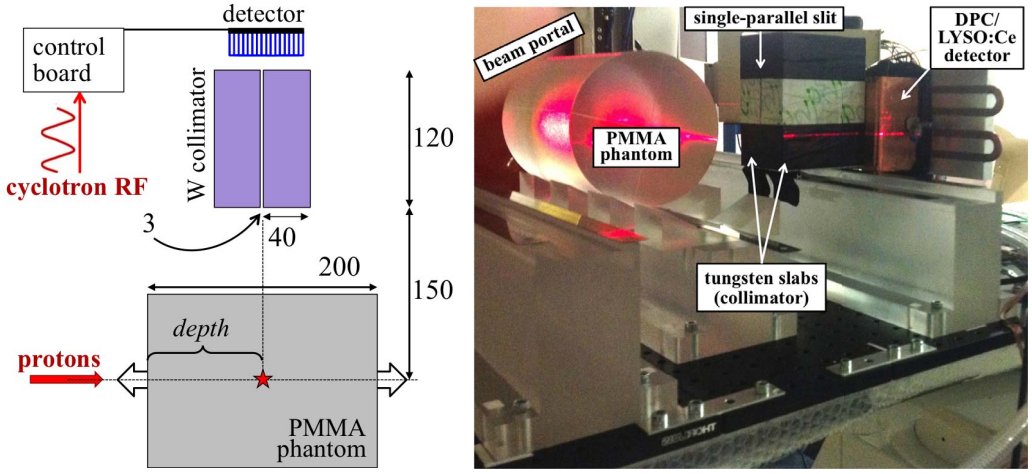

Fig. 1. Left: schematic of the measurement setup (top view), with distances displayed in millimeters. The distance between the collimator back-surface and the front-surface of the scintillators was about 12 mm. The intersection between the slit mid-plane and the beam axis (★) gives the position of emission of the PG rays being imaged. Right: photograph of the experimental setup. The LYSO:Ce detector was mounted on a breadboard; both collimator and phantom were placed on PMMA support rails.

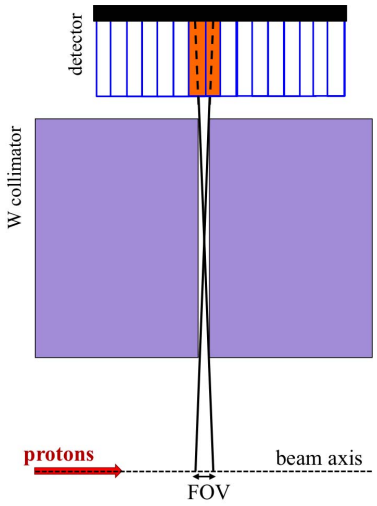

Fig. 2. Zoomed-in view of Fig. 1(left) (not to scale), showing that only the two rows of crystals represented in orange (corresponding to one row of DPC-chips) are directly exposed to the collimated gamma rays emitted from the FOV in the beam axis.

The collimator was made of two tungsten slabs, each with dimensions of 12 cm × 4 cm × 15 cm (Fig. 1). The collimator left uncovered a column of eight DPC-chips with a total length of 6.6 cm. The slit width of 3 mm corresponded to a field of view (FOV) of 10.5 mm at the beam axis (excluding septa penetration), which upon projection onto the back-surface of the 22-mm long crystals yielded a width of 4.7 mm. Since: 1) the center of the slit was aligned with the center of the uncovered DPC-chips in the beam direction and 2) each chip is subdivided into 2 × 2 pixels with a 4-mm pitch, with each pixel being coupled to a single crystal, the amount of crystals that were exposed to the collimated gamma rays was 2 (in the beam axis, Fig. 2) × 16 (slit axis) = 32.

Although only one column of DPC-chips was left uncovered by the slit, the whole detector (with an area of 6.6 cm × 6.6 cm) was actively measuring. This enabled the clustering of multiple-chip events (arising due to intercrystal Compton scattering) by means of a coincidence window acting on the detector level, so as to increase the detection efficiency [3].

III. TOF-Shift Calibration Curve

Time calibration was implemented offline by post-processing experimental in-beam time spectra. The clock skews between the DPC chips that were left uncovered by the collimator were accounted for, to ensure proper time alignment [18]. These skews were derived from per-chip time-spectra previously measured in [3] using the knife-edge slit collimator and a five times higher total amount of delivered protons, providing better statistics. The chips considered here for timing measurements were aligned with the (knife-edge) slit axis. The prompt peak position was determined for each chip as the TS corresponding to the maximum of the interpolated time histogram. For interchip time calibration, considering chips in a given row exposed to the slit, a fixed beam energy was utilized, resulting in negligible influence of proton transit time on the time calibration. Hence, the time differences between the chips arise from the different inter-chip clock skews and from the different PG TOF arising from gamma rays impinging on the detector with different tilting angle (Fig. 3). These two effects result in a constant time difference between any two given chips, which was corrected for by aligning the peak positions of the per-chip time histograms.

The time spectra obtained at phantom depths proximal to the proton range are presented in Fig. 4, post time-skew correction. These time spectra show that the prompt peak sits on a slowly rising slope of neutron-related background counts, which peak at TSs posterior to the corresponding prompt peak. The intensity of this background shoulder increases with increasing phantom depth, which is expected due to the fact that neutrons are mostly forward-projected. Background counts occurring before the PG peak are most likely originating from previous

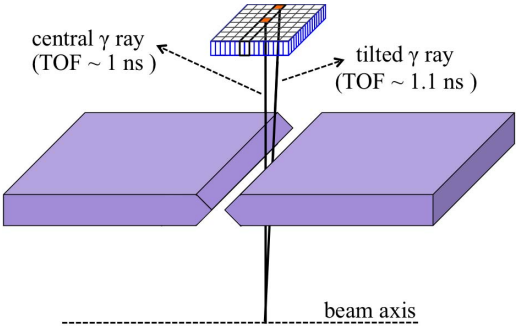

Fig. 3. Schematic of the experimental setup used for calculating the time skews between the sensors within the same row aligned with the slit axis. The maximum path difference between two detected gamma rays yields a TOF difference of about 100 ps.

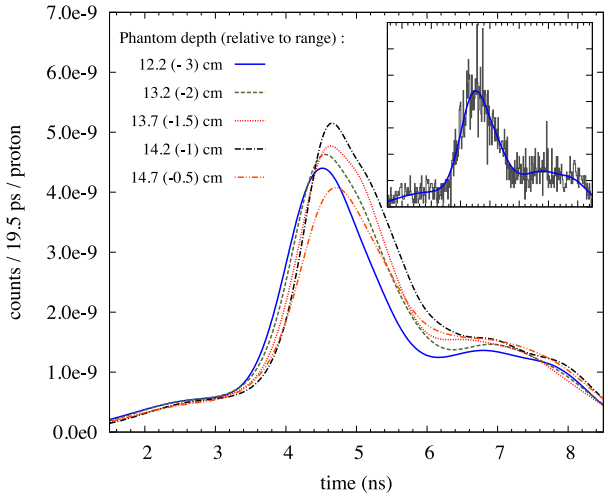

Fig. 4. Time-spectra of DPC-chip-events registered over the entire detector segment uncovered by the single-parallel-slit (~66-mm length), relative to an arbitrary phase of the cyclotron RF cycle, post time-skew correction and with a low-energy cutoff of 3 MeV on chip level. The time spectra were measured at five different phantom depths [Fig. 1(left)] proximal to the proton range. The differences in proton travel time in air between the various measurements were taken into consideration. The smooth curves correspond to KDE results obtained from the measured data. The inset shows an exemplary data histogram obtained at 12.2-cm depth (black) and the corresponding KDE curve (blue), plotted on the same horizontal/vertical axis as the main graph.

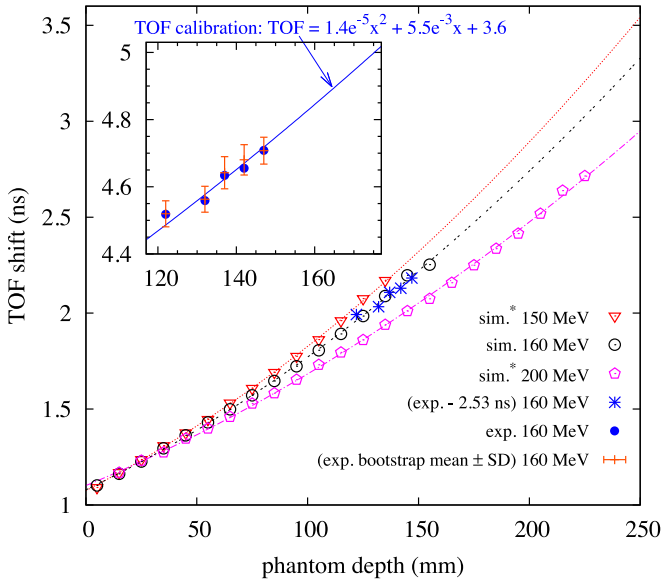

Fig. 5. Simulated and measured TOF shifts, as a function of phantom depth, for the beam energy used in this experiment (160 MeV) and for higher and lower proton energies (simulations only, after [2]*). The simulated TOF shifts correspond to a start time when the proton is launched 1 cm before the phantom and a stop time at a detector located at 30 cm from the beam axis, while the measured ones (inset) were obtained relative to an arbitrary phase of the RF cycle and are displayed as in Fig. 4. Also shown are the curves fitted to the simulated TOF shifts and the TOF-shift calibration curve used to apply TOF discrimination (inset). The latter is equal to the double-dashed curve plus an arbitrary offset of 2.53 ns that minimized the square sum of the residuals relative to the experimental TOF shifts. The inset also shows the mean and SD of the experimental TOF shifts, obtained by bootstrapping.

proton bunches [2], as the range of neutron arrival times is relatively large.

The prompt peak position is a function of the proton penetration depth, due to the finite proton velocity within the phantom. In order to accurately pinpoint the TOF shift value, the histograms of the time spectra were interpolated to reduce the influence of statistical noise. Fitting of the time spectra with predefined functions that model both PG curve and background, as previously done in [3], was found to yield insufficiently accurate results. Possible reasons for this are as follows.

1) The TS distribution of PGs is mostly determined by the proton-bunch time-width, which is approximately Gaussian-shaped but may not be completely symmetric [12].
2) Additional asymmetry in the PG-TS distribution may arise due to scattered PGs.
3) The shape of the distribution of background TSs is not entirely known and difficult to model.

Therefore, the time spectra were interpolated using the kernel density estimation (KDE) class available in the ROOT data analysis framework, based on works by [1], [10], and [15]. KDE works on the raw TS data to estimate, in a nonparametric way, a probability density function of arbitrary shape. Default options and parameter rho (equal to 1.0) were used. The latter affects the kernel width and thus the degree of smoothing. KDE was also used to derive the time skews between the DPC-chips, from measurements previously performed using a knife-edge slit collimator, as described above.

The inset in Fig. 4 shows a KDE result in comparison to the corresponding measured histogram. Note that the KDE function converges to zero at the edges. Also note that the counts at the edges of the original time spectra ($\lesssim$ 1 ns) were artificially reduced due to the facts that: 1) there was a limit in the range of possible TS values output by the DPC-chips (the TS range was smaller than the 9.4 ns period of the RF-cycle [3]) and 2) the time spectra from different chips were summed after being shifted relative to each other (to correct for the time skews).

The TOF shifts for the five phantom depths prior to the proton range were obtained from the TSs corresponding the maxima of the KDE curves. These TOF shifts are represented by the closed circles in Fig. 5(inset). They are compared to simulated TOF shifts in the main panel of Fig. 5 (open circles), which were obtained using Geant4 (version 9.3, package

QGSP_BERT_HP) in a similar way as in [2]. The TOF shifts reported by Biegun *et al.* [2] are also shown. These correspond to proton energies above (200 MeV) and below (150 MeV) the energy of 160 MeV used in the current experiments.

The simulated TOF shifts for proton penetration depths between zero and the proton range $R = 15.2$ cm were used to derive the overall shape of the TOF calibration curve. In a first step, a second-order polynomial function was fit to the simulated TOF shifts (as in [2]). Subsequently, the TOF-shift calibration curve was determined by fitting that polynomial function plus a constant offset to the experimental TOF shifts, with the offset as the only free parameter. Fig. 5(inset) shows this calibration curve in the range of phantom depths at which the measurements were done.

The uncertainty in TOF-shift determination was estimated using the technique of bootstrapping and the results are presented by the red error bars in Fig. 5(inset). From each time spectrum considered, a set of 100 time-spectra were generated, each of which was derived by randomly sampling, with replacement, the original data set of TS values, for a number of times equal to the original data size. The TOF-shift was subsequently derived for every bootstrap sample after interpolation by KDE, and the corresponding mean and standard deviation (SD) values were calculated. It can be seen in Fig. 5(inset) that: 1) the uncertainty is relatively small; viz., less than 50 ps on average and 2) the TOF-shift values derived without bootstrapping are very close to the average values derived by bootstrapping.

IV. Event Processing

Energy calibration, cluster processing (using a 5-ns wide paralyzable coincidence window on detector level) and crystal assignment ("winner-takes-all") were applied as described in detail in [3]. Energy calibration was based on point source measurements up to an energy of 4123 keV.

The energy spectra from events originating at phantom depths proximal and distal to the proton range $R = 15.2$ cm, with and without TOF discrimination, are presented in Fig. 6. Fig. 7(top) shows the intensity maps of crystal assignment corresponding to the same measurements, for the case without TOF discrimination. Whereas Fig. 7 shows events registered on the whole detector surface, the energy spectra (Fig. 6) include only events assigned to the 32 crystals that were exposed directly to the collimated radiation. Those crystals are indicated by the dashed rectangles in Fig. 7(top). The remaining crystals were located behind the collimator.

Fig. 7 shows that a relatively high amount of background counts is registered at the detector pixels located most closely to the beam entrance point in the phantom. This can at least partly be attributed to the fact that PG rays emitted near the phantom entry point and traveling to crystals located at the upstream side may enter the collimator through its side surface instead of its front surface, resulting in a shorter path through the collimator material and, therefore, less efficient shielding of these PG rays. However, it is to be emphasized that such events are not expected to play a significant role in the analysis of PG profiles and background rejection presented in the next section, since only counts that are assigned to crystals uncovered by the collimator slit will be taken into account.

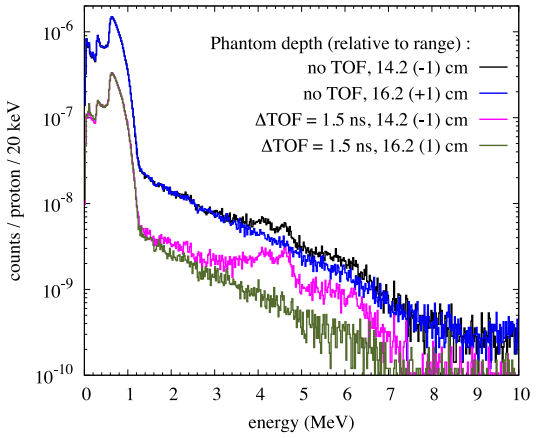

Fig. 6. In-beam energy spectra measured with (pink and green) and without (black and blue) TOF discrimination, having the FOV of the single-parallel-slit collimator centered at phantom depths equal to $R - 1$ cm (pink and black) and $R + 1$ cm (green and blue), where $R = 15.2$ cm is the proton range in PMMA. The data were acquired for the highest amount of delivered protons.

V. PG Intensity Profiles and Background Rejection

PG intensity profiles with and without TOF discrimination were obtained by integrating the counts assigned to the 32 directly exposed crystals (see Fig. 7), for each longitudinal position along the beam axis at which a measurement was done. As an example, Fig. 8 shows the results obtained after applying an energy acceptance window ranging from 3 to 7 MeV, with and without TOF.

A. Signal-to-Background Ratio

The counts detected at phantom depths distal to the Bragg peak are expected to be due to background, i.e., counts resulting from prompt neutrons (which may generate gamma rays in, e.g., the collimator and detector materials), scattered gamma rays, and gamma rays penetrating through the tungsten parts of the collimator without being absorbed. Essentially the same can be said about counts assigned to detector pixels behind the collimator. Therefore, the background before TOF discrimination can be estimated by interpolation, i.e., by averaging the amount of counts assigned (without TOF selection) to the two columns of DPC-chips that are closest to the column of DPC-chips left uncovered by the collimator slit (as indicated in Fig. 7), namely left and right to it.

The resulting background intensity profile is represented by the red squares in Fig. 8. We observe an increase in background intensity with increasing phantom depth, which is attributed to the fact that the neutrons generated in proton-induced nuclear reactions are emitted mostly in the forward direction at the proton energies of interest. As expected, the background thus estimated accounts for almost all of the counts (black circles) registered beyond the falloff region (i.e., at depths $\geq R + 1$ cm). The small difference between the black circles and the red squares may primarily be due to

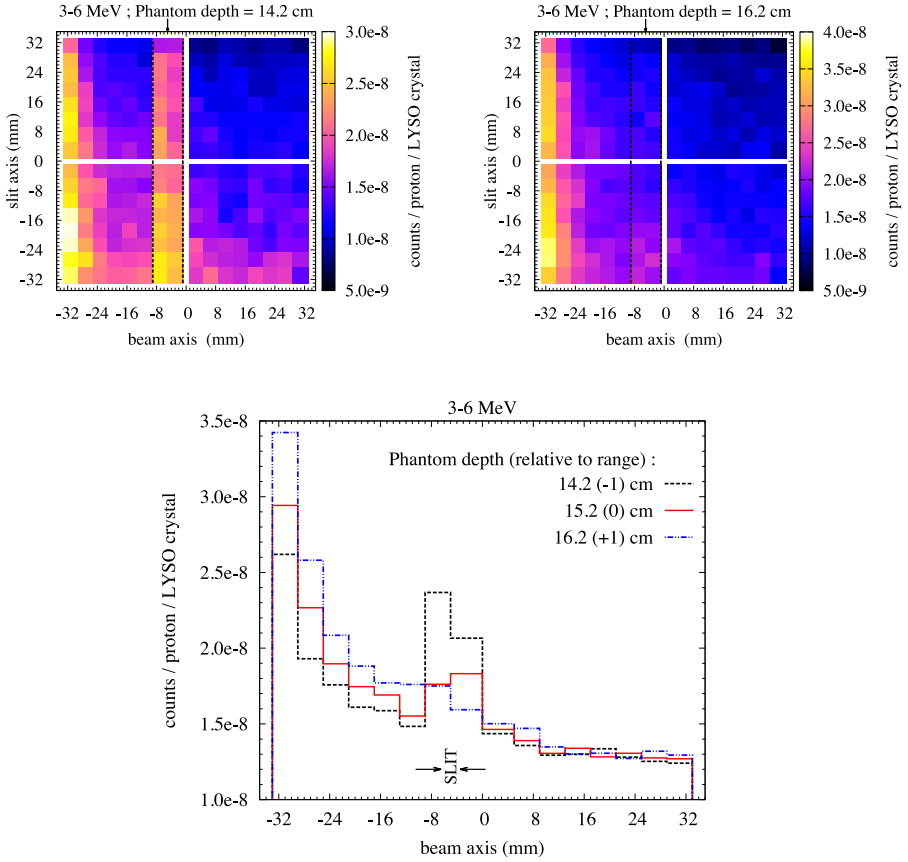

Fig. 7. Intensity maps of crystal assignments (top) and projection profiles along crystal columns parallel to the slit (bottom), of events registered in the energy window between 3 and 6 MeV without TOF discrimination, having the FOV of the single-parallel-slit collimator centered at phantom depths of $R - 1$ cm (black) and $R + 1$ cm (blue), as well as at R (projection profile only). The two crystal columns contained by the dashed line (top graphs) were exposed to the collimated radiation. The slit opening is indicated by the arrows on the bottom graph. The data corresponding to the 2-D intensity maps were acquired with 5× higher statistics, in terms of total delivered protons.

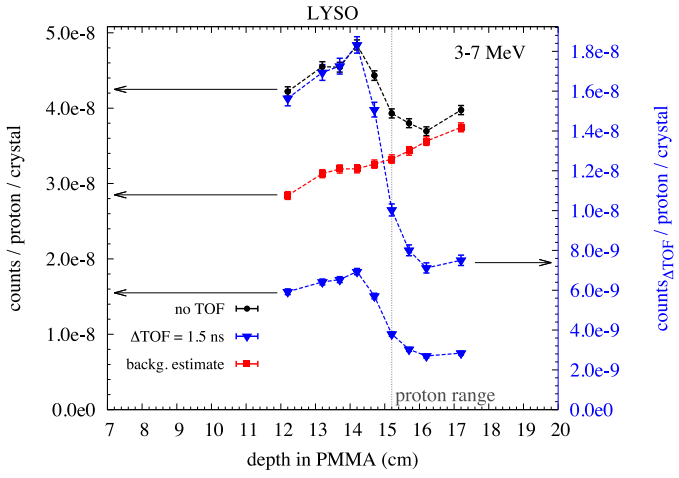

Fig. 8. Profiles obtained without (back circles) and with (blue triangles) TOF discrimination, as well as the estimated background before TOF discrimination (red squares, see text for details). The profile with TOF discrimination is displayed on the same scale as the other profiles (left-axis), as well as on a separate scale (right-axis), chosen such that the maxima of the profiles with and without TOF coincide. The dashed vertical line indicates the proton range R. The error bars correspond to one SD, as expected on the basis of Poisson statistics.

gamma photons that are either generated (by neutrons) or scattered in the distal part of the phantom and that subsequently travel through the collimator slit toward the detector.

Given the above, a pragmatic approach to compare the S/B ratios with and without TOF discrimination for different energy windows is to estimate them directly from the corresponding intensity profiles (i.e., from the blue triangles or black circles in Fig. 8, respectively), using the following equation:

$$\mathrm{S/B} = \frac{C_{R-1\mathrm{cm}} - C_{R+1\mathrm{cm}}}{C_{R+1\mathrm{cm}}} \tag{1}$$

where $C_{R-1\ \mathrm{cm}}$ and $C_{R+1\ \mathrm{cm}}$ represent the counts at $R - 1$ cm and $R + 1$ cm, respectively, corresponding to the maximum and the minimum of the measured intensity profiles.

The method described in (1) is similar to the one previously used in [3]. Therefore, we will use this method in this paper to facilitate comparison of the results. Moreover, given that estimates of the proton range are typically derived from analysis of the falloff region of the PG intensity profile near the Bragg peak, (1) may be seen as an estimate of S/B relevant to the intended application. For completeness, it should be noted that this definition assumes the same background level at $R - 1$ cm and $R + 1$ cm, whereas in reality the background intensity increases with increasing depth (red squares in Fig. 8). Hence, (1) can be seen as a conservative estimate of S/B in the region of interest.

B. Slope-Over-Noise Ratio

The slope-over-noise ratio in the fall-off region of the PG profiles is considered a useful figure-of-merit of the performance of the collimator in estimating the proton range in a homogeneous phantom, as it takes into account the influence of both signal-to-noise ratio in the measured PG profiles and collimator resolution. For example, if we consider a simple estimator of the Bragg peak position, based on the depth ζ at which the PG falloff profile intersects a certain threshold level, then the uncertainty in ζ equals the ratio of the noise and the slope of the PG falloff profile at that point. It is acknowledged that such a simple range estimator is not necessarily applicable in clinical situations, due to, e.g., range degradation and straggling arising from tissue heterogeneities and/or beam-modifying devices. However, the proposed figure of merit is a measure of the ability of the collimator to resolve gradients in the PG profile, an important endpoint in PG camera design.

To determine the slope from the PG profiles measured with the single-parallel slit, we fitted a complementary error function (sigmoid curve) to the PG profiles obtained with the single-parallel slit. This procedure is similar to that used in [3], except that a linear baseline was used instead of a constant offset in addition to the sigmoid function, as this appeared to result in a better fit. The figure-of-merit was subsequently calculated as

$$\text{FOM} = \left.\frac{dn}{\sqrt{n}dz}\right|_{\zeta=\text{inflexion point}} \tag{2}$$

where the noise is approximated by the square root of the number of counts at the inflection point of the sigmoid fit, n, z is the depth in the phantom, and dn/dz is the slope evaluated at the inflection point ζ.

C. Performance Optimization

Table I shows the S/B and FOM values for various energy acceptance windows and with/without TOF background rejection. TOF discrimination appears to improve the S/B ratio by a factor of ∼6 for the energy window of 2–6 MeV, and by a factor of ∼5 for the energy windows of 3–6 and 3–7 MeV. In fact, these S/B improvements are somewhat underestimated, as some TOF selection is still present in the "no-TOF" profiles due to the fact that events with TSs at the edges of the 9.4-ns long RF wave period (not more than 30% of the total period) were not registered [3].

We also observe an improvement of the FOM by using TOF discrimination, namely by a factor of ∼2.2, ∼1.7, and ∼1.8 for the energy window of 2–6, 3–6, and 3–7 MeV, respectively. Interestingly, while there is no significant difference between the S/B ratios corresponding to the 3–6 and 3–7 MeV energy windows with TOF discrimination, the FOM is slightly better for the latter window (3.1 mm^{-1} versus 2.9 mm^{-1}). This is attributed to the corresponding increase in the total number of counts by about 13%, which gives rise to a higher absolute slope and reduced statistical fluctuation.

VI. Conclusion

In this paper, we have used a scanning parallel-slit collimator to measure time spectra, energy spectra, and intensity profiles of PG rays emitted at various depths along a 160-MeV proton pencil-beam in a PMMA phantom. The collimator was placed in front of a detector based on matrices of LYSO:Ce crystals read out by arrays of DPCs. The scanning parallel slit collimator may be seen as a simple model of a multislat collimator, especially in what concerns the timing information. We applied different energy windows and a shifting TOF window to the measured intensity profiles. Depending on the energy window used, TOF discrimination appeared to improve the S/B ratio by a factor of ∼5–∼8. As a consequence, the slope-over-noise ratio in the falloff region of the PG profile, improved by a factor of ∼1.7–∼2.6. The best FOM value was obtained for the energy window 3–7 MeV in combination with TOF discrimination.

A. Scanning Parallel Slit Versus a Knife-Edge Slit

The present results can be compared to those obtained in [3], in which the same scintillation detector was used, in combination with a knife-edge slit collimator made from the same material (tungsten), and in which essentially the same irradiation setup was used. In view of clarity, we note that the data from [3] was not reanalyzed in the current fashion of a shifting TOF discrimination approach, i.e., a TOF calibration curve was not used to explicitly to take into account the kinematics of the protons traversing the medium. Instead, in that work the position of the PG peak was determined for each die independently, taking implicitly into account all delays together, i.e., interdie time skews, proton travel time, and the PG TOF. Considering that the proton bunch width is of the same order of the TOF shift in the range of depths analyzed (i.e., in the falloff region of the PG profile), we do not expect that the different nuances in the implementation of TOF discrimination can compromise this comparison (see also Section VI-B).

From the comparison of the two collimators, the following observations can be made.

1) The energy spectra obtained in this paper (Fig. 6) reveal more clearly marked spectral features in the energy range between ∼3 and ∼7 MeV, such as the 4.4-MeV peak. This suggests a lower relative contribution from gamma rays scattered within the collimator or phantom. This may indeed be expected because: 1) the thickness of the collimator material between the beam and the detector is much larger in this paper and 2) the collimator acceptance angle is much narrower, allowing fewer scattered photons to reach the detector.
2) The time spectra obtained in this paper (Fig. 4) show a somewhat lower ratio between the prompt peak intensity and the background baseline, suggesting a higher relative contribution from neutron-related background counts. Also this is expected, because the detector is placed much closer to the collimator in which the neutrons may create gamma rays that can be detected. Here,

TABLE I
ESTIMATED S/B RATIO (1) AND FIGURE OF MERIT [FOM, (2)] FOR DIFFERENT ENERGY WINDOWS AND WITH/WITHOUT TOF DISCRIMINATION. THE IMPROVEMENT FACTORS OBTAINED BY USING TOF DISCRIMINATION ARE DISPLAYED FOR BOTH S/B AND FOM AS THE RATIO OF THE CORRESPONDING VALUES WITH AND WITHOUT TOF

Energy window (MeV - MeV)	S/B		Improvement factor	FOM (mm^{-1})		Improvement factor
	No TOF	TOF	$(S/B_{TOF})/(S/B_{No\ TOF})$	No TOF	TOF	$(FOM_{TOF})/(FOM_{No\ TOF})$
1 - 6	0.04(1)	0.30(2)	8(2)	-0.53	-1.4	2.6
2 - 6	0.17(2)	1.02(5)	5.8(7)	-1.3	-2.8	2.2
3 - 6	0.33(3)	1.62(8)	5.0(5)	-1.7	-2.9	1.7
3 - 7	0.31(2)	1.57(8)	5.1(5)	-1.7	-3.1	1.8

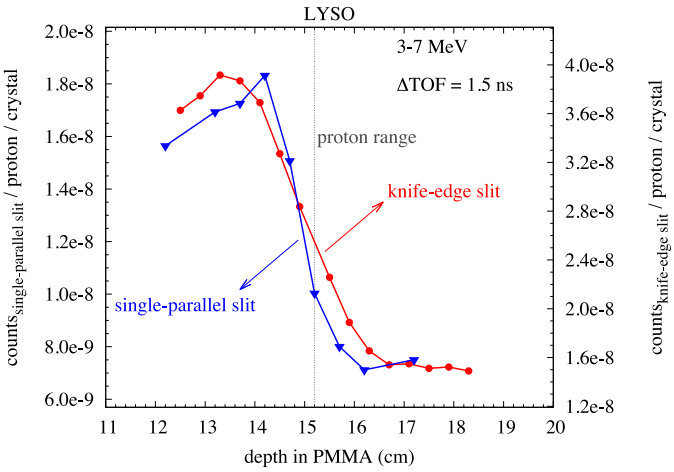

Fig. 9. Comparison of intensity profiles measured in essentially identical experimental setups (including approximately the same distance between the beam axis and the detector front face, as well as between the beam and the collimator) with the current scanning single-parallel slit and the knife-edge-slit reported by [3]. Only events falling within an energy window of 3–7 MeV and **D**TOF = 1.5 ns were accepted in both cases.

it is to be noted that LYSO:Ce crystals are more sensitive to gamma rays than to neutrons.

3) Comparable S/B ratios of approximately ∼1.6 can be achieved with both collimators, if a low-energy cut-off of 3 MeV in combination with TOF discrimination is applied for optimal S/B in both cases. The following considerations may help to explain this observation. Both beam-collimator distance and total collimator mass (and volume) are similar in both experiments. This would be expected to result in a similar exposure of the collimator to neutrons as well as a similar production of secondary gamma-rays. However, the thickness of collimator material in between the beam axis and the detector is much higher in the single-parallel slit case (12 cm versus 4 cm for the knife-edge experiment). This may imply a higher attenuation of secondary gamma rays and, consequently, a lower detected background in the case of the single-parallel slit. At the same time, however, the lower efficiency (due to geometrical considerations) of the single-parallel slit also reduces the number of PG rays (i.e., signal) reaching the detector. In view of the above considerations, it is interesting to note that poorer S/B ratios are observed for the scanning parallel slit for low-energy cutoffs < 3 MeV than for the knife-edge slit collimator (e.g., ∼1.0 versus ∼1.3, respectively, for the energy window 2–6 MeV, with TOF). These observations are consistent with the hypothesis that a larger fraction of the background counts is due to gamma rays generated in the collimator by neutrons, taking into account that many of these gamma quanta may undergo Compton scattering in the collimator before reaching the detector. Also, the relative differences between the S/B ratios obtained with and without TOF discrimination are larger for the scanning parallel slit for such energy thresholds, meaning considerably worse S/B without TOF discrimination (e.g., 0.3 parallel slit versus 0.5 knife-edge slit, for the energy window 3–7 MeV). Hence, both TOF discrimination and the selection of the low-energy cutoff appear to be more crucial for the single-parallel-slit collimator, in comparison to the knife-edge slit collimator.

4) Finally, Fig. 9 shows the effect of the improved spatial resolution obtained in the current experiment, compared to the knife-edge slit collimator (data from [3]). Note that in the figure the two profiles are plotted with different scales (single-parallel slit in the left *y*-axis, knife-edge slit in the right *y*-axis) allowing for visual comparison of the relative slopes, which may be seen as a measure of the collimator resolution. By normalizing both profiles to a maximum intensity of 1, it can be shown that the relative slope of the parallel slit collimator is a factor of 1.8 better than that of the knife-edge slit. Interestingly, a simple geometrical calculation of the point resolution assuming infinitely dense collimators indeed predicts a factor of 1.8 improvement in spatial resolution for the parallel-slit compared to the knife-edge slit (6.8 mm versus 12 mm, respectively). Such improved resolution may increase the capability to detect, among others, deviations in the shape of the distal falloff arising in the irradiation of highly heterogeneous media. However, with the current single-parallel slit setup this comes at the expense of a reduction of the total number of counts by a factor of about two (see Fig. 9).

We further compare the two collimators in terms of the FOM given in (2). It appears that the FOM of the single-parallel slit is a factor ∼1.2 better than that of the knife-edge slit, for all of the energy windows 2–6, 3–6, and 3–7 MeV, in combination with TOF discrimination. Specifically, the FOM values of the knife-edge slit are -2.3 mm^{-1}, -2.4 mm^{-1}, and -2.5 mm^{-1}, respectively. Without TOF discrimination, the FOM of the knife-edge slit is better than that of the single-parallel slit by a factor ∼1.3 for the energy window 2–6 MeV, and approximately the same (factor ∼1.0) for a low energy threshold of 3 MeV. For completeness, the FOM values of the knife-edge slit without TOF are -1.7 mm^{-1} (2 MeV – 6 MeV), -1.6 mm^{-1} (3 MeV – 6 MeV), and -1.8 mm^{-1} (3 MeV – 7 MeV). The FOM values for the single-parallel slit can be found in Table I. It is noted that these values were obtained for the same number of incident protons. Given that the FOM puts both system resolution and statistical noise into equation, these results indicate that the better resolution of the single-parallel slit could still be beneficial, despite the relatively high statistical noise arising from its lower efficiency.

B. Limitations and Outlook

The work presented has some limitations. It should be noted that the results on S/B values and system resolution and efficiency obtained with the scanned parallel-slit cannot be directly translated to the more complex case of a multislat collimator. The multisepta of a multislat collimator, interleaved by air slabs, would result in increased septa penetration by oblique gamma rays, which may degrade the system spatial resolution with respect to the single parallel-slit case. On the other hand, a multislat collimator will have a higher efficiency, while the reduced amount of collimator material in the vicinity of the detector will reduce the number of (n, γ) reactions, resulting in fewer background events.

Finally, one might argue that shifting the TOF window may have limited effect in the present case, due to the small range of phantom depths measured (5 cm in total and 3 cm until the proton range), given the minimum width of the TOF acceptance window as determined by the width of the proton bunches. Instead of a shifting TOF window, a fixed window could be used, which could be made somewhat broader to account for proton motion. In this paper, the time span of no overlap between the two outermost TOF windows corresponded to ∼1/3 of the window width. However, this paper aims to show how the shifting TOF window can be applied in general. The impact of shifting the TOF window is significantly greater when measuring profiles over the whole proton range [2]. Further work is necessary to demonstrate experimentally the impact of the shifting TOF approach in a situation where a broad FOV is imaged, i.e., the whole proton range.

To conclude, this paper presents the necessary steps to experimentally implement the concept of a shifting TOF window for background discrimination, using pixelated detectors and a parallel-slit collimator. The methods described here can be applied straightforwardly to a multislat collimator. Our results indicate that, when using optimized energy and TOF discrimination, the PG profiles obtained with a single parallel-slit collimator yield approximately the same S/B ratio as previously obtained with a knife-edge slit camera, at approximately the same distance from the beam axis. Furthermore, the single-parallel slit shows potential advantages in terms of the accuracy of estimating Bragg peak positions from PG profiles. In particular, the slope-over-noise ratio was found to be higher than for the knife-edge slit collimator. Future studies are necessary to: 1) verify experimentally whether these conclusions remain valid for a full-scale multislat collimator, whether a better slope-over-noise ratio indeed translates into better performance in range estimation in clinical practice and to 2) further optimize the collimator properties, so as to achieve the best compromise between resolution, sensitivity, and S/B ratio.

ACKNOWLEDGMENT

The authors would like to thank the team of IBA, namely S. Henrotin, G. Janssens, D. Prieels, F. Roellinghoff, J. Smeets, and F. Stichelbaut, as well as E. Clementel (iMagX Project, Universiteì Catholique de Louvain) for assisting the measurements; Philips Digital Photon Counting, in particular C. Degenhardt, Y. Haemisch, R. Schulze, and B. Zwaans for the fruitful discussions and help with the hardware and software implementations that made the synchronized measurements possible; IBA team at WPE, in particular A. Varga Sampedro and P. Vidal Caravaca for their precious support; J. Koning, K. Langelaan, and W. van Goozen (DEMO, TU Delft) for the technical support with the measurement setup; and the team of the high-performance computing Milipeia cluster (University of Coimbra). They would also like to thank S. Seifert, G. Borghi, and V. Tabacchini (TU Delft) for the fruitful discussions, and M. Sarilar (INAA Laboratory, TU Delft) for preparing the Na-24 radioactive source.

REFERENCES

[1] B. Jann, *Univariate Kernel Density Estimation*, KDENS document, ETH Zurich, Zürich, Switzerland, Aug. 2007. [Online]. Available: http://fmwww.bc.edu/repec/bocode/k/kdens.pdf

[2] A. K. Biegun *et al.*, "Time-of-flight neutron rejection to improve prompt gamma imaging for proton range verification: A simulation study," *Phys. Med. Biol.*, vol. 57, no. 20, pp. 6429–6444, 2012.

[3] P. Cambraia Lopes *et al.*, "Time-resolved imaging of prompt-gamma rays for proton range verification using a knife-edge slit camera based on digital photon counters," *Phys. Med. Biol*, vol. 60, no. 15, pp. 6063–6085, 2015.

[4] C. Degenhardt *et al.*, "The digital silicon photomultiplier—A novel sensor for the detection of scintillation light," in *Proc. IEEE Nucl. Sci. Symp. Med. Imag. Conf. Rec.*, 2009, pp. 2383–2386.

[5] C. Degenhardt *et al.*, "Performance evaluation of a prototype positron emission tomography scanner using digital photon counters (DPC)," in *Proc. IEEE Nucl. Sci. Symp. Med. Imag. Conf. Rec.*, Anaheim, CA, USA, 2012, pp. 2820–2824.

[6] T. Frach *et al.*, "The digital silicon photomultiplier—Principle of operation and intrinsic detector performance," in *Proc. IEEE Nucl. Sci. Symp. Conf. Rec.*, Orlando, FL, USA, 2009, pp. 1959–1965.

[7] T. Frach, G. Prescher, C. Degenhardt, and B. Zwaans, "The digital silicon photomultiplier—System architecture and performance evaluation," in *Proc. IEEE Nucl. Sci. Symp. Conf. Rec.*, Knoxville, TN, USA, 2010, pp. 1722–1727.

[8] C. Golnik *et al.*, "Range assessment in particle therapy based on prompt γ-ray timing measurements," *Phys. Med. Biol.*, vol. 59, no. 18, pp. 5399–5422, 2014.

[9] Y. Haemisch, T. Frach, C. Degenhardt, and A. Thon, "Fully digital arrays of silicon photomultipliers (dSiPM)—A scalable alternative to vacuum photomultiplier tubes (PMT)," *Phys. Procedia*, vol. 37, pp. 1546–1560, Oct. 2012.

[10] W. Härdle, A. Werwatz, M. Müller, and S. Sperlich, "Nonparametric density estimation," in *Nonparametric and Semiparametric Models* (Springer Series in Statistics). Heidelberg, Germany: Springer, 2004. [Online]. Available: https://doi.org/10.1007/978-3-642-17146-8_3

[11] C. H. Min, H. R. Lee, C. H. Kim, and S. B. Lee, "Development of array-type prompt gamma measurement system for *in vivo* range verification in proton therapy" *Med. Phys*, vol. 39, no. 4, pp. 2100–2107, 2012.

[12] K. Parodi *et al.*, "Random coincidences during in-beam PET measurements at microbunched therapeutic ion beams," *Nucl. Instr. Methods Phys. Res. A Accelerators Spectrometers Detectors Assoc. Equip.*, vol. 545, nos. 1–2, pp. 446–458, Jun. 2005.

[13] M. Pinto *et al.*, "Design optimisation of a TOF-based collimated camera prototype for online hadrontherapy monitoring," *Phys. Med. Biol.*, vol. 59, no. 24, pp. 7653–7674, 2014.

[14] F. Roellinghoff, *et al.*, "Real-time proton beam range monitoring by means of prompt-gamma detection with a collimated camera," *Phys. Med. Biol.*, vol. 59, no. 5, pp. 1327–1338, 2014.

[15] D. W. Scott, *Multivariate Density Estimation: Theory, Practice, and Visualization*. New York, NY, USA: Wiley, 1992.

[16] J. Smeets, *et al.*, "Prompt gamma imaging with a slit camera for real-time range control in proton therapy," *Phys. Med. Biol.*, vol. 57, no. 11, pp. 3371–3405, 2012.

[17] M. Testa *et al.*, "Monitoring the Bragg peak location of 73 MeV/u carbon ions by means of prompt gamma-ray measurement," *Appl. Phys. Lett.*, vol. 93, Sep. 2008, Art. no. 093506.

[18] H. T. van Dam, G. Borghi, S. Seifert, and D. R. Schaart, "Sub-200 ps CRT in monolithic scintillator PET detectors using digital SiPM arrays and maximum likelihood interaction time estimation," *Phys. Med. Biol.* vol. 58, no. 10, pp. 3243–3257, 2013.

[19] H. T. van Dam, S. Seifert, and D. R. Schaart, "The statistical distribution of the number of counted scintillation photons in digital silicon photomultipliers: Model and validation," *Phys. Med. Biol*, vol. 57, no. 15, pp. 4885–4903, 2012.